Higher-order statistical analysis of short wind wave fields

Guillemette Caulliez, Charles-Antoine Guérin

Higher-order statistical analysis of short wind wave fields

Guillemette Caulliez[1] and Charles-Antoine Guérin[2]

Received 23 December 2011; revised 11 April 2012; accepted 16 April 2012; published 2 June 2012.

[1] Observations of along-wind surface wave profiles were made in the large Marseille-Luminy wind wave tank for a broad range of wind and fetch conditions. The processing of high resolution camera snapshots enables us to carry on a thorough statistical analysis of wind wave geometrical properties. We consider distinctively the four different wind wave fields characterized by a comprehensive image analysis in the range of capillary-gravity to gravity scales. This set of data makes it possible to describe and discuss the behavior of the distribution of wave heights, longitudinal wave slopes and curvatures in terms of their second- and higher-order moments as well as a function of the dominant wave scale. We calculate the autocorrelation and related functions and evidence the self-similar nature of wind wave fields. We also derive a simple and universal expression for the structure functions of third (skewness) and fourth (kurtosis) order which are needed for the simulation of sea radar return in the microwave regime.

Citation: Caulliez, G., and C.-A. Guérin (2012), Higher-order statistical analysis of short wind wave fields, *J. Geophys. Res.*, *117*, C06002, doi:10.1029/2011JC007854.

1. Introduction

[2] Today, satellite remote sensing opens the possibility of characterizing the ocean surface both at global scale and at fine resolution, using active or passive instruments. Following the recent improvements in techniques and theories, links have been established between the cross-section of the sea surface associated with the respective backscattered or emitted microwave signals and a large number of oceanic parameters, such as wind speed and direction, wave heights and slopes, wave spectrum, surface current, temperature and salinity, etc. However, the success of the inversion procedure relies crucially on an accurate phase resolving statistical description of the sea surface topography. In this respect, non-Gaussian characteristics of short wind waves are of primary importance, as they have a strong influence on the microwave radar return. For instance, they are responsible for the so-called electromagnetic bias in altimetry [*Srokosz*, 1986] and the upwind/downwind asymmetric response of scatterometers [e.g., *Liu et al.*, 1997]. Furthermore, when intimately related to breaking phenomena, non-Gaussian wave statistics are responsible for the "sea spikes" in the sea clutter [e.g., *Jessup et al.*, 1990] and the anomalous Doppler response [e.g., *Thompson et al.*, 1991].

[3] Electromagnetic sea surface interaction theories used in the context of ocean remote sensing generally consist in single scattering models [e.g., *Valenzuela*, 1978; *Elfouhaily and Guérin*, 2004] in which the backscattered cross-section depends directly on the distribution of surface elevations, slopes and curvatures as well as the distribution of two-point height differences. In most applications, these distributions are assumed Gaussian to render the calculations tractable. However, many theoretical studies have shown the impact of non-Gaussian wave statistics on sea surface scattering properties [*Chen et al.*, 1992, 1993; *Chapron et al.*, 2000; *Liu et al.*, 2000; *Guérin*, 2002; *Engen et al.*, 2006; *Bourlier*, 2004; *Mouche et al.*, 2007; *Nouguier et al.*, 2010, 2011].

[4] Very little is actually known about the higher-order statistics of short wind wave geometrical properties and their space variations. The departure from the Gaussian scheme generally considered is limited to the skewness and kurtosis of wave heights and slopes, involving the third and fourth moments of the distributions. The reference results remain these obtained by *Cox and Munk* [1954] during an historical experiment in which the distribution of slopes were derived from the analysis of sea surface photographs. Such studies have been actively pursued and the early findings have been confirmed by further observations using various types of optical or microwave sensors both in natural conditions [*Bréon and Henriot*, 2006; *Shaw and Churnside*, 1997; *Walsh et al.*, 1998; *Vandemark et al.*, 2004] and in laboratory [*Wu*, 1977; *Huang et al.*, 1984; *Jähne and Riemer*, 1990; *Fedorov et al.*, 1998]. At the same time, to describe these observations, several hydrodynamical models have been elaborated [*Huang et al.*, 1983; *Srokosz*, 1986; *Liu et al.*, 1997].

[5] As a matter of fact, the distributions of short wind wave height and slopes have been classically derived from time measurements made by probes located at a fixed position and more recently from remote observations as these

[1]Mediterranean Institute of Oceanography, CNRS 7294/IRD 235/AMU/USTV, and Centre National de la Recherche Scientifique, Marseille, France.

[2]Mediterranean Institute of Oceanography and Université du Sud-Toulon-Var, La Garde, France.

Corresponding author: C.-A. Guérin, Mediterranean Institute of Oceanography, Ave. de l'Université, BP 20132, F-83957 La Garde, France. (guerin@univ-tln.fr)

0148-0227/12/2011JC007854

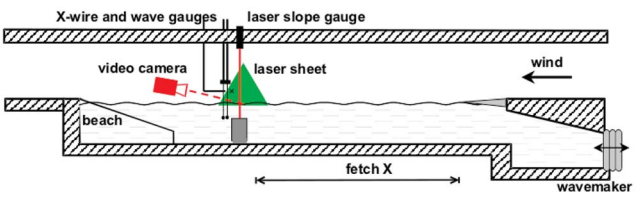

Figure 1. Schematic view of the experimental arrangement and the instrumentation set up in the large Marseille-Luminy wind wave tank for wave visualizations. The camera is oriented perpendicularly to the laser sheet and the air channel glass side window, looking down with a tilt angle of 8°.

quoted above. Accordingly, despite the issues raised by the high-slope cut-off introduced by the optical limits of the measuring devices, the distributions of heights and slopes of short wind wave fields are by now rather well documented. However, since the pioneering observations by *Schooley* [1954], measurements of short wind wave curvatures remain quite scarce and of coarse resolution [*Wu*, 1971, 1977; *Nosov and Pashin*, 1990; *Ermakov et al.*, 1997]. In addition, there are very few experimental results pertaining to the so-called structure functions, which are the moments of the two-point differences of surface elevations. A detailed experimental study of the temporal and spatial structure functions has been carried out by *Lukaschuk et al.* [2009] and *Nazarenko et al.* [2010] to determine the scaling laws at small lags but it concerns only random gravity wave fields generated by a wavemaker in a water tank. For this purpose, it should be emphasized that the structure functions, in particular these of order 3 and 4 denoted respectively the skewness and the kurtosis functions, are of primary importance for simulating the radar return from the sea surface from approximate scattering models [e.g., *Mouche et al.*, 2007]. Hence, to progress in this domain, direct spatial measurements of the geometrical wind wave features are still needed. As a first attempt to fill this gap, this work presents a statistical analysis of the geometrical properties of short wind wave fields derived from spatial wave measurements performed along the wind direction by means of a novel surface-imaging technique.

[6] Non-Gaussian statistics of wave slopes and wave curvatures are strongly dependent on the spatial distribution of short wind waves over longer dominant or intermediate-scale waves, as shown for instance by *Plant* [2003]. As a consequence, the precise description of the sea surface roughness properties is not an easy task because ripples or small-scale surface disturbances are generated by several processes dependent on wind speed. The first mode of generation of short waves is directly related to the viscous shear stress exerted by wind at the sea surface as modeled by *Miles* [1962] and *Van Gastel et al.* [1985]. When observed at short fetches in laboratory, such centimeter-scale wind-generated waves are homogeneously distributed at the water surface but in open seas, their full development is highly sensitive to wind speed steadiness and the presence of longer waves. The development of parasitic ripples at the crest of steep gravity-capillary waves is the second but efficient source of very short scale wave disturbances at the water surface [*Ermakov et al.*, 1986; *Zhang*, 1995]. As theoretically described by *Hung and Tsai* [2009], they mainly grow on the forward face of the primary waves, leading to an increase of the related wave slope skewness. At last, micro-breaking and breaking wave phenomena are also responsible for the formation of small-scale roughness at the crest of steep gravity-capillary or gravity waves, but their basic features as scales, patchiness or time persistence are far from being well-characterized up to now [*Kudryavtsev and Johannessen*, 2004]. Small-scale wind wave fields thus result from a complex interplay of these various phenomena. Accordingly, one can easily presume that the higher-order statistics of the geometrical properties of the sea surface would exhibit significant variations with wind, making their characterization quite challenging. Therefore, to get some basic trends about the dependency on wind of such quantities, this work takes advantage of laboratory space observations to describe more extensively the related features of well-identified short wind wave fields. It should be noted that our results pertain to one-dimensional characteristics of waves since the technique is based on profile imaging, which here gives access to properties of the wave field in the wind direction. This is, however, a first series of results which shows the potential of photographic imaging techniques for the statistical characterization of short wind waves.

[7] First, the paper will present in section 2 the experimental arrangement adopted for wave observations and in section 3, the main characteristics of the wind wave fields then selected. The wave image processing and analysis will be described in more details in section 4. Finally, the outcomes obtained from the one- and two-point statistical analysis of short wind wave field features will be discussed in sections 5 and 6.

2. Description of the Data Basis

[8] The observations were carried out in the large Marseille-Luminy wind-wave facility which is made of a 40 m long, 2.6 m wide and 0.9 m deep water tank and a recirculating air flow channel with a test section of about 1.5 m in height, as described in more details in *Coantic and Bonmarin* [1975] and depicted schematically in Figure 1. Steady winds varying between 1 and 14 m s^{-1} are generated by an axial fan located in the recirculation flume. The air flow channel which includes divergent and convergent sections, turbulence grids and a test section of slightly-enlarged height, is specially designed to obtain a low-turbulence homogeneous flow at the entrance of the water tank and a constant-flux air boundary layer over the water surface. In addition, to avoid generation of large-scale air flow disturbances just over the surface boundary layer, a weakly-inclined flexible device was fixed at the edge of the bottom floor of the air channel to smooth the junction between this solid floor and the water surface for all wind speed conditions. At the end of the water tank, a permeable beach damps the wave reflection. The instruments for wind and wave measurements were set up at a fixed position located at the 28 m fetch test section of the channel which is equipped with glass windows. Then, to adjust the measuring fetch, the upwind water surface was covered by a thin floating plastic sheet of variable length.

[9] Visualizations of surface wave profiles along the wind direction were performed by means of a vertical plane light

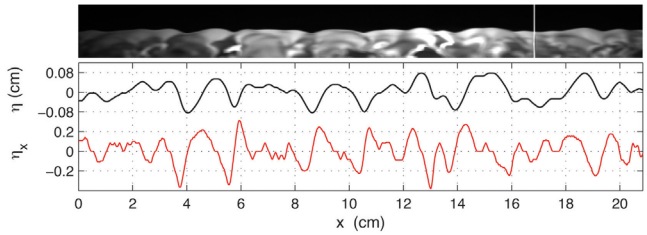

Figure 2. Regime 1: Typical wave profile observed in the large wind-wave tank at 2.0 m fetch and 5.5 m/s wind speed. (top) Typical image viewed from the side by the camera, the wind blowing from left to right. (bottom) Wave contour extracted from the image and the associated longitudinal wave slope.

sheet and a high-resolution monochrome digital video camera looking down through the air channel glass side window with a tilt angle of 8°. The imaging technique that is quite similar to that employed by *Diorio et al.* [2009] and the wave contour detection method are described in detail in G. Caulliez (Dissipation regimes for short wind waves, submitted to *Journal of Geophysical Research*, 2012). In short, the light sheet located in a longwise vertical plane at a distance of 40 cm from the tank sidewall, was generated by a 4 W Ar^+ laser coupled with an optical fiber and a cylindrical lens. The water was seeded by fluorescent dye for sharpening the light contrast of the air-water interface. The images of 2000 × 640 pixels sizes, which corresponds approximately to a field of view of 23 cm in the horizontal direction with a pixel resolution of 0.116 mm, were captured by a MegaPlus ES 4.0 video camera at a frame rate of 15 Hz. The exposure time was adjusted in the 3 to 6 ms range, decreasing with dominant wave phase speed increase. To extract the surface wave profiles from the recorded images, an original software based on a Canny edge detection method was developed. The latter is based on the detection of the local luminance gradient maxima using two successive gradient magnitude thresholds. The surface contour lines are then identified as the first maxima found when moved vertically from the air to the water flow. The various stages in data filtering and smoothing will be detailed and analyzed more extensively in section 4. In addition to wave visualizations, direct measurements of wave height and wave slopes in the along- and crosswise directions were made by means of one capacitance wave gauge located just at the downwind end of the camera field of view as well as two longwise-aligned capacitance wave probes and a single-point laser slope optical system located respectively at 46 and 28 cm crosswise to the laser sheet. The laboratory-made slope measuring system is based on the detection of the refraction angle of a He-Ne laser beam at the water surface using a Fresnel lens and a 2D position sensor, as first designed by *Lange et al.* [1982]. The nonlinear but isotropic response of this device was determined by carrying out careful calibration before the experiments and its cut-off at high slopes was estimated at ±40° for the working water tank depth. The air flow velocity field and the wind drag exerted at the water surface were monitored by a Pitot tube and X-wire probes. The experiments were performed at 4 fetches between 2 and 26 m, and for 6 or 7 wind speeds ranging from 3 to 10 m/s. For each couple of wind and fetch conditions, six to ten series of 300 images were recorded in parallel with the wind velocity, wave elevation and surface slope signals.

3. Wind Wave Field Observations

[10] When wind blows at the water surface, waves of dominant wavelength ranging from 3–6 to 80 cm as function of wind speed develop with fetch along the tank. Previous observations enable us to distinguish various types of wind-waves depending primarily on wavelength and resulting from a change in the balance between capillary and gravity restoring forces.

[11] In this range of wave scales, four regimes have been identified, associated with four types of wave shape and ensuing mode of wave dissipation (see *Caulliez and Collard* [1999] and *Caulliez* [2011] and for a more detailed description G. Caulliez (submitted manuscript, 2012)). The first regime corresponds to the capillary-gravity waves generated by wind at very short fetches. These waves of small wavelength and tiny height, typically less than 5 cm and 1 mm, exhibit wave profiles with characteristic round crests and sharper troughs as displayed in Figure 2. The wave motions however are widely distributed in scale, height and wave propagation direction, thus making the wave field highly variable both in space and in time. Their development at the water surface results from a selective wave amplification mechanism due to the combined action of wind shear flow and viscous dissipation. At the next stage (regime 2) of wind-wave growth occurring at immediately longer fetch, the wave field is composed of dominant gravity-capillary waves propagating obliquely on both sides to the wind direction (with angles close to ±30°) and then forming conspicuous rhombic patterns at the water surface. As seen in Figure 3, these waves of wavelength less than about 10 cm, present generally an asymmetric crest with a round bulge at the wavefront and a train of capillary ripples developing ahead. For such short gravity-capillary waves, nonlinear resonant interactions appear to be the main mechanism of dissipation as a significant part of the dominant wave energy is transferred to these well-formed parasitic capillaries [*Tsai and Hung*, 2010]. Wave fields of longer dominant wavelength (regime 3), up to 20 cm, exhibit roughly similar features, i.e., they are mostly composed of three-dimensional gravity-capillary waves with asymmetric round crest and capillaries propagating on their forward face (Figure 4). Note however that the rhombic wave patterns are much less regular, the wave ridges becoming shorter and propagating at smaller oblique angles to the wind direction [*Caulliez and Collard*, 1999]. The wave fields also present two other main differences. First, the capillary ripples are noticeably shorter and of

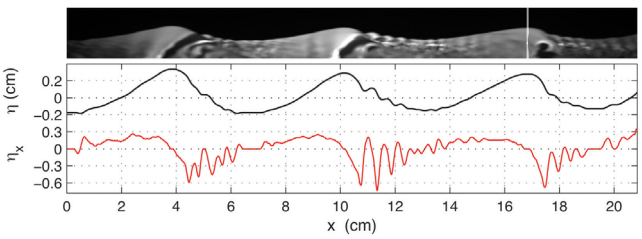

Figure 3. Regime 2. Typical wave profile at 6 m fetch and 5.0 m/s wind speed: idem as regime 1.

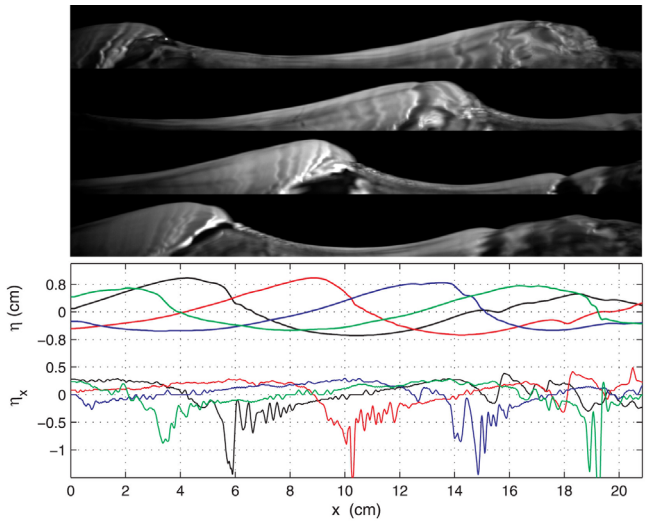

Figure 4. Regime 3. Longitudinal wave profiles observed at 6 m fetch and 8.0 m/s wind speed: idem as regime 1 except that (top) four images and (bottom) the related four wave contours and x wave slope signals are given.

smaller height, such scales decreasing as the dominant wavelength increases. Second, dominant waves with very steep crest wavefront are found occasionally. This steepening phenomenon can be followed by a localized surface disruption at the crest bulge toe. Such small crest breakdown, generally denoted micro-breaking, generates on the forward face of the wave, short-lived irregular disturbances and more long-lived trains of large-scale ripples. By creating surface roughness as well as small-scale turbulent motions in water, these events thus contribute in another way to dominant wave dissipation. The fourth regime corresponds to the development by wind of short-crested gravity waves of wavelength roughly higher than 20 cm. These wave fields present generally characteristic Stokes-shaped waves with rather pyramidal crests and flat troughs. These surface motions vary both in height, scale and wave propagation direction. From time to time however, microbreaking phenomenon develops at the crest of the highest waves inside the wave groups. Such event manifests again when the crest wavefront steepens and breaks down, creating disturbances and wavy motions at the air-water interface as well as turbulence in water. However, the turbulent velocity fluctuations appears not energetic enough for generating large pressure fluctuations at the water surface and thus prompting the bubble formation. For wind speeds higher than 7 m/s, more dramatic wave crest breakdown akin to plunging wave breaking may also occur for the steepest waves, as displayed in Figure 5. This phenomenon is initiated by the development of an almost overturning wave crest associated with the growth of a very pronounced bulge on the upper forward wave face. The crest protrusion then gives rise to a small water jet projecting out from the wavefront face and impacting the water surface ahead of the crest. This plunging microjet generates in turn a small water splash-up impacting the water surface further downstream. This wave crest breakdown develops until the fluid ejections degenerate into a patch of turbulence spreading inside the upper water flow and marked at the surface by small protuberances and wavy roughness. During this event, the intensity of the crest collapse controls the bubble formation. As a matter of fact, only isolated bubbles can be noticed at the water surface when observed two-decimeter scale wave fields while whitecaps and quite dense bubble plumes are formed when longer waves break in a more chaotic way at the strongest wind speeds.

4. Retrieval of Water Surface Geometrical Characteristics

[12] As explained previously, the extraction of the water surface contours from the various sets of images enables to get series of raw wave height snapshots along a longitudinal section of roughly 23 cm in the x wind direction. Considering a reference coordinate system with the horizontal axis x oriented in the wind direction and the vertical axis z oriented upwards, the wave elevation $\eta(x)$ is then defined as the excursion of the profile from the mean horizontal plane estimated for the whole set of images captured in the same wind and fetch conditions. In addition, the wave slope component in the wind direction corresponds to the first derivative η_x of the wave profile and the wave curvature in this direction γ is related to the second derivative η_{xx}:

$$\gamma(x) = \frac{\eta_{xx}(x)}{(1 + (\eta_x(x))^2)^{3/2}}. \quad (1)$$

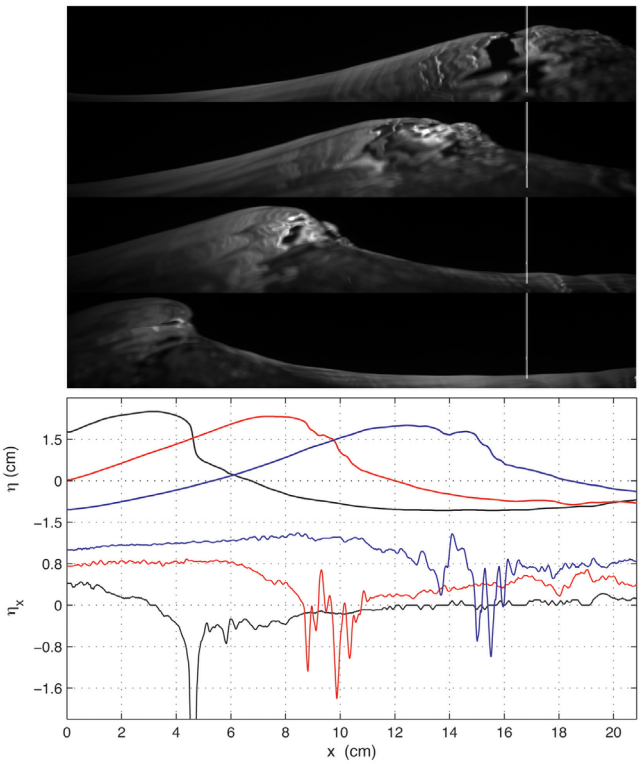

Figure 5. Regime 4. Longitudinal wave profiles observed at 13 m fetch and 8.0 m/s wind speed: idem as regime 1 except that four images and the related four wave contours and x wave slope signals are given respectively at the top and bottom plots. For sake of clarity, the wave slope zero is shifted by 0.4 from one signal to the other. The plunging breaking wave has a wavelength of approximately 25 cm.

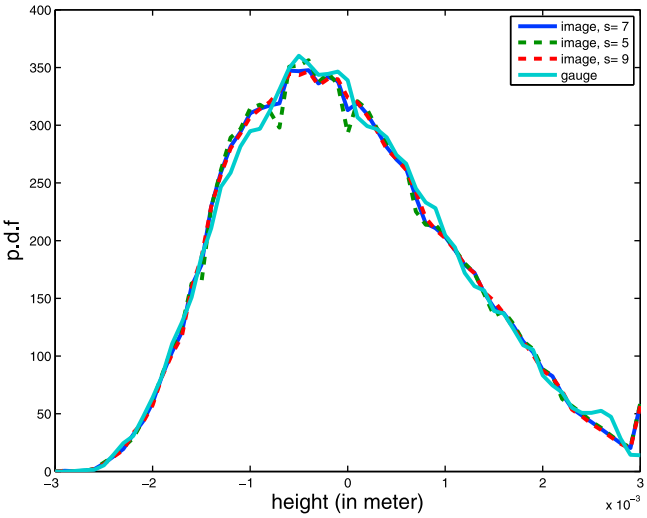

Figure 6. Comparison of the p.d.f. of height estimated from image-extracted wave profiles with those derived from capacitance wire gauge measurements for regime 2. The distributions obtained with three different window widths of the Gaussian filter used to smooth wave profiles are shown, the curve plotted with a continuous line corresponding to the selected width ($s = 5, 7, 9$ is given in number of pixels and corresponds to the standard deviation of the gaussian filter). The distribution of height is robust to the change in the smoothing parameter.

These first two derivatives are estimated by centered finite differences of wave elevations. To estimate these three quantities it is crucial to first determine whether wave profiles extracted from the digital camera images actually correspond to the "true" profiles and with which resolution. The wave imaging technique raises two main difficulties. First, the snapshots are blurred due to wave motion during the exposure time. Given the typical phase velocity and the selected exposure time we estimate the blurring distance to about 15 pixels. Blurring has the effect to replace a sharp surface contour by a strip. Deblurring is realized while using the contour detection algorithm which detects the maximum of the luminance gradient in the strip and restore an "average" position of the edge. For surface waves however, the dye particles at the water surface move along the surface streamlines, so nonlinearities or bias which might be introduced in the profiles by this averaging procedure look negligible. Only the related decrease of the surface luminance gradient magnitude may inject a little noise, of order of one pixel, in the retrieved wave profiles. In the end, it is difficult to assess the final longitudinal resolution which can be achieved after this processing. All that can be said is that the resolution is no worse than 1.8 mm and probably better. Note that such a wave scale corresponds to capillaries of about 300 Hz in frequency and 0.04 s in $\exp(-1)$ viscous lifetime, i.e., waves of very weak probability of manifestation. In that respect, this fact was corroborated by radar measurements in Ka-band and optical observations that show by comparison the contribution of submillimeter waves to the total mean square slope is very small [*Vandemark et al.*, 2004]. This means that we will miss only, if significant, the contribution of one or two millimeter long waves to the slope and curvature distribution. The second source of error is the discretization of the recorded signal in both longitudinal and vertical directions at the pixel resolution, that is 0.116 mm. Hence the profiles consist in piecewise constant functions with small jumps corresponding to a multiple of this basic unit. The quantization effect, on one hand, has negligible impact on the statistical distribution of elevation, which ranges over several orders of magnitude larger than the pixel value. However, it has a dramatic effect on the estimated values of slope and curvature. Therefore, a crucial aspect of the image processing is smoothing. Given the very small value of the pixel resolution, smoothing can be performed without deteriorating the initial wave contour resolution of 1.8 mm in the wind direction. As the higher-order statistical surface roughness properties may, however, depend strongly on the smoothing procedure, the later has to be fixed on the basis of physical considerations. A way to do this is to compare *a posteriori* the estimated probability density functions (p.d.f.) of height, slope and curvature obtained after smoothing with direct measurements of these quantities made by means of single-point high resolution wave probes. This comparison has been made for regime 2 with various reference distributions determined as follows:

[13] 1. The reference distribution of wave height has been derived from the time series of surface elevation $\eta(x_0, t)$ given by the wave gauge located at a fixed position x_0 just at the end of the field of view of the camera and recorded simultaneously with the image capture.

[14] 2. The reference distribution of the longitudinal wave slope η_x has been derived directly from measurements made by the single-point laser slope gauge. However, comparatively with the reference height distribution, these measurements were not made in the laser sheet plane but 28 cm crosswise, which may entail some discrepancies between both estimations owing to the limited length of the time records. Therefore, the wave slope distribution has also been inferred from the time derivative of the wave height signal η_t using the relationship $\eta_x = -1/c\ \eta_t$ in which c is the mean dominant wave phase speed estimated by means of a cross-correlation method using the time signals of the two nearby wave gauges. Note that such a method is based on the assumption that the wave field propagates along the wind direction in a frozen way. This is a reasonably good approximation for the gravity-capillary wave fields with parasitic capillaries as observed in regime 2 because the dominant fields are composed of two trains of symmetric oblique waves. As a result, these composite fields propagate in the wind direction, and this even for scales in the capillary range but in average owing to the related intermittent wave occurrence.

[15] 3. The distribution of the longitudinal wave curvature has been deduced in a similar way on the basis of the formula $\eta_{xx} = -1/c\ \eta_{xt}$, using the time derivative of the wave slope signal and the mean dominant wave phase speed c.

[16] Then the smoothing procedure has been defined in the following way: to obtain a smooth profile with at least two derivatives, a running average of the raw data has been performed using a Gaussian window with various standard deviations s. The first and the last pixels of the smoothed profiles have been also discarded to avoid side effects. When compared the p.d.f. of the different wave shape characteristics and the corresponding reference distributions, the best

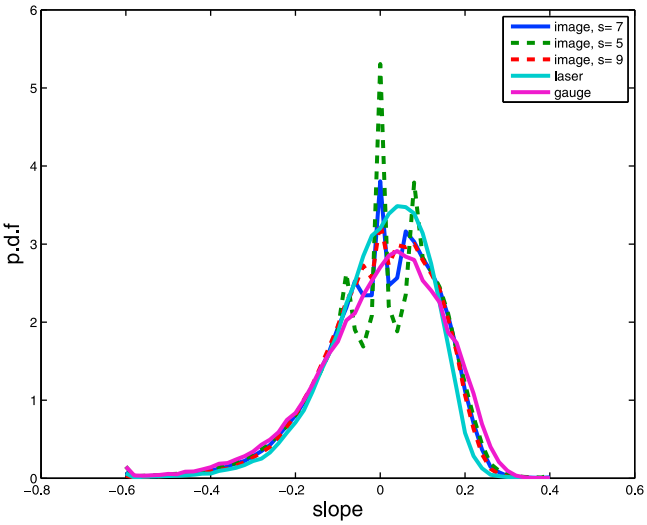

Figure 7. Comparison of the p.d.f. of the longitudinal wave slope estimated by derivation of wave profiles extracted from images with these computed directly from the x-component laser slope gauge signal or indirectly by derivation of the capacitance gauge wave height signal for regime 2. The distributions obtained with three different window widths of the Gaussian filter used to smooth wave profiles are shown, as in Figure 6. Unlike the wave height distribution, the shape of the wave slope distribution is very sensitive to the smoothing parameter. Insufficient smoothing ($s = 5$) does not smear the unphysical peaks resulting from the wave profile quantization. The negative slope values are mainly observed on the forward face of dominant waves and the positive ones on the backward face.

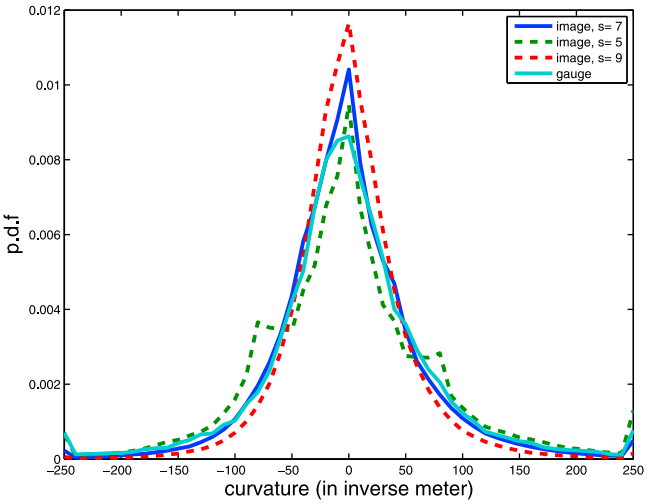

Figure 8. Comparison of the p.d.f. of longitudinal curvature estimated by two successive derivation of wave profiles extracted from images with those computed indirectly by derivation of the laser slope gauge signal for regime 2. The distribution derived from the image wave profile depends dramatically on the smoothing parameter with an optimal s value of 7. The positive curvature values are observed on the convex wave face with a curvature center in the air while negative ones on the concave face.

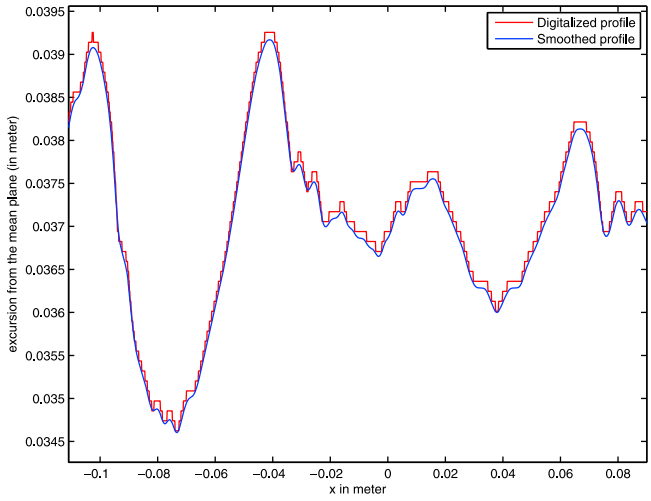

Figure 9. Typical snapshot of a digitalized raw profile plotted together with its smoothed version.

compromise for retrieving both high and small values in wave slope and wave curvature was then found when s was fixed at a value of 7 pixels, which means that the profiles are smoothed out over an effective weighted window of about 3 mm. These results are shown in Figures 6, 7 and 8. Note again that for facilitating the comparison, both wave height data series are centered around their space and time averages (i.e., $\langle \eta \rangle = 0$). As expected, the distribution of height is found robust to the value of the smoothing parameter s. Regarding the slope distribution derived from the images and displayed in Figure 7, the three peaks visible in the central part of the curve consist in artifacts of the quantization of both the p.d.f slope intervals and the wave slope values which remain even after smoothing. The same remark holds for the curvature distribution (Figure 8). As found, the optimal smoothing parameter is $s = 7$. In that case it is noticeable that a very good agreement is found between image and gauge estimations of both the slope and curvature distribution, especially for the overall shape and at the tails of the curves. The maximal slope obtained after smoothing then depends on the maximal height in pixels N_H of the vertical wavefronts observed in the raw profile series and can be estimated to approximately $0.06\ N_H$. The highest jumps observed in the raw profiles analyzed here reach about 50 pixels (Figure 5), thus the maximal slope is of the order of 3 (i.e., 70°). To illustrate the effect of the smoothing procedure adopted in this work on the wave height profile, a snapshot of the raw profile and its corresponding smoothed version is shown in Figure 9.

5. One Point Statistical Distributions

[17] In this section, the properties of the marginal distributions of elevation, slope and curvature are examined for one wind and fetch condition characteristic of each wave field regime (see Table 1). In the literature, the statistical properties of wave height and wave slopes as observed in laboratory have been extensively analyzed, but similar results concerning wave curvatures are much scarcer and limited to a small number of wind or fetch conditions. In addition, as described in section 3, this investigation is focused on the statistical features of well-identified wave fields of different

Table 1. Cumulants of Wave Elevation, Longitudinal Slope and Curvature for the Different Regimes

	Regime			
	1	2	3	4
Wind (m/s)	5.5	5	8	8
Fetch (m)	2	6	6	13
Dominant wavelength (cm)	3	6	14	23
Elevation (η in mm)				
rms height $\kappa_2^{1/2}$	0.4	1.0	3.5	6.7
Skewness coefficient λ_3	0.06	0.38	0.42	0.43
Excess kurtosis λ_4	0.00	−0.28	−0.44	−0.33
Slope (arctan(η_x) < 40 deg)				
rms slope	0.12	0.13	0.18	0.20
Skewness coefficient	−0.4	−0.8	−0.6	−0.3
Excess kurtosis	1.0	1.3	0.8	0.3
Slope (arctan(η_x) < 60 deg)				
rms slope	0.12	0.13	0.19	0.21
Skewness coefficient	−0.5	−0.8	−0.9	−0.6
Excess kurtosis	1.0	1.4	2.1	2.1
Curvature (η_{xx} < 1000 m^{-1})				
rms curvature	63 ± 3	60 ± 4	65 ± 5	70 ± 5
Skewness coefficient	0.6	0.3	0.2	0.1
Excess kurtosis	6 ± 1	8 ± 1	15 ± 1	17 ± 1

scales and undergoing different types of wave dissipation. Therefore, to better distinguish an eventual evolution of the various distributions under study across the different wave regimes, both scales of such functions have been renormalized using the corresponding standard deviation (denoted σ in the text whatever the variable) to obtain plots with dimensionless units. Note also that the observed wind wave fields have reached a steady state in the sense that their statistical properties do not vary with time. However, at such short fetches, they are non-homogeneous in space and so, their dimensional and non-dimensional statistical properties might strongly depend on fetch.

5.1. Heights

[18] The p.d.f. of surface elevation for the four wave regimes are shown in Figure 10 in linear scales. At the smallest wind and fetch condition (regime 1), the distribution of elevation is found to be approximately Gaussian, corroborating the random behavior of the capillary-gravity wave field generated at a very small fetch by moderate wind. For increasing winds and fetches, a significant departure from the Gaussian distribution is observed, with a shift of the central peak towards negative values then balanced by a more abrupt decay at the highest negative height. This shape accounts for the strong asymmetry between wave troughs and crests observed classically for Stokes-like gravity waves, but also for gravity-capillary waves as short as 6 cm as clearly seen here. Note that the distribution asymmetry increases from regime 2 to regime 3, i.e., when the dominant wavelength increases, but decreases a little for regime 4 owing to the development of wind-generated small-scale roughness all over the dominant waves at the highest wind speed conditions.

5.2. Slopes

[19] The p.d.f. of longitudinal slope are shown in Figure 11 in semi-logarithmic scales, in reference to the normal distribution. For small slope values (less than 2σ), the distribution exhibits quite a similar shape for all regimes, following approximately a Gaussian trend specially at negative slopes

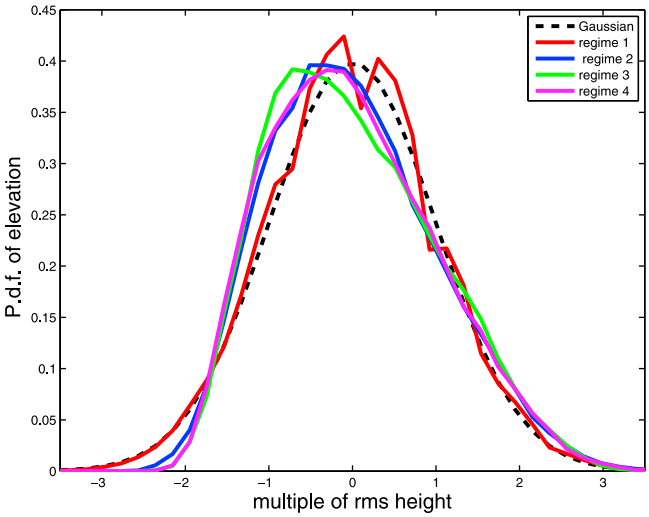

Figure 10. Normalized p.d.f of wave height estimated for the various wave regimes observed in the Marseille-Luminy wind-wave tank and plotted in reference to the Gaussian distribution. The x-axis is scaled with the respective standard deviation displayed in Table 1.

(generally mostly found at wave fronts). For positive slopes as typically observed on the rear of wave crests, the departures from the Gaussian curve are a little more pronounced. In particular, the higher probability to observe very small positive values can be noticed, then associated with a rapid fall-off of the curves around 2σ. This behavior appears directly linked to the front-back asymmetry of short gravity-capillary or short gravity wave profiles, thus accounting for the gentle slopes observed at the rear of the wave crest as strikingly displayed in Figures 3 and 4. However, the slope distribution of capillary-gravity wave fields typical of regime 1 again better fits the normal law. In this case, one can notice

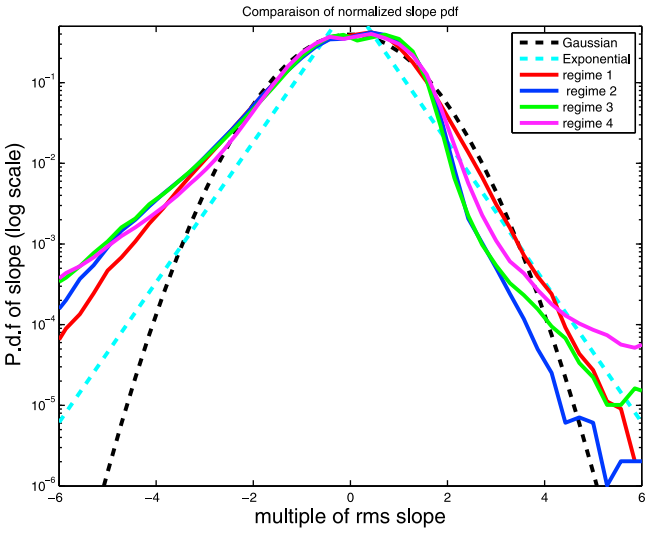

Figure 11. Normalized p.d.f of longitudinal wave slope estimated for the various wave regimes and plotted in semi-logarithmic scales together with the reference Gaussian distribution. The horizontal axis is scaled relatively to the respective slope standard deviation.

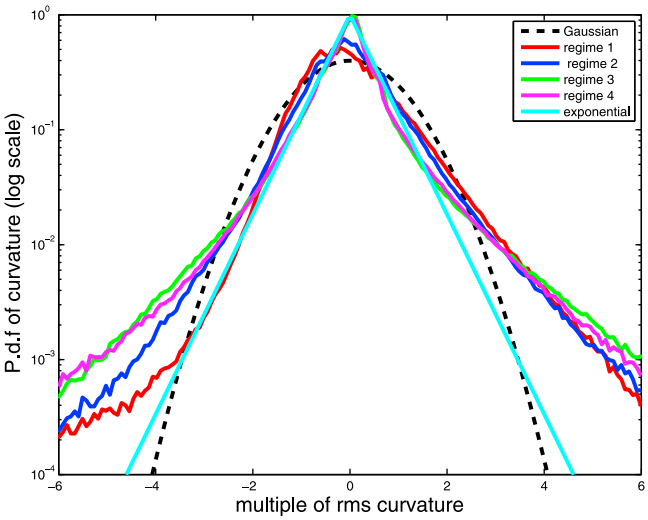

Figure 12. Normalized p.d.f of longitudinal wave curvature estimated for the various wave regimes and plotted in semi-logarithmic scales together with the reference Gaussian and exponential distributions.

a few peaks for slopes very close to zero, which are a remaining sign of the quantization of wave elevation as mentioned in section 4. The digitalized profiles indeed possesses an exaggerated number of zero slopes (due to the staircase plateaus) as well as a discrete set of values corresponding to the different slopes attainable with a step function. This effect that is not completely smeared by the smoothing procedure, is more pronounced for tiny waves of small steepness. At large wave slopes, the various p.d.f. have strongly asymmetric tails with a rather faster decay for positive slope values and a slow decay for negative ones. This feature is specially marked for regimes 2 and 3 owing to the conspicuous steepening of wave fronts and the development there of high-slope parasitic capillaries, as illustrated in Figures 3, 4, and 5. At the highest wind speeds observed here for regimes 3 and 4, the positive tail found at slopes greater than 3.5σ exhibits a transition revealed by a significant slow down of the decrease of the distribution. This behavior is induced by the development of small-scale wave roughness generated directly by wind over the whole water surface for winds higher than 6 m/s about. Capillary-gravity ripples of quite high slopes (very similar as these generated in regime 1) then ruffle both sides of the dominant wave crests. Note that for regime 4, the phenomena at the origin of the tail for negative slopes differ from these detected for regimes 2 and 3 inasmuch as the development of parasitic capillaries at the crest wavefront diminishes drastically for such longer dominant gravity waves. In such a case, in addition to the ripples generated directly by wind, it should be rather ascribed to the increasing occurrence of small-scale random surface disturbances generated by wave micro-breaking and breaking.

[20] Power-law decay or alpha-stable distributions are often invoked to describe the tail of the wave slope distribution [*Voronovich and Zavorotny*, 2001; *Guérin*, 2002; *Joelson and Néel*, 2008]. However, a closer inspection of the data indicates that the slope distribution decreases much faster than a power-law since it takes a quasi-linear form in a semilogarithmic representation, making it actually closer to an exponential distribution. For very large positive slopes ($\eta_x > 3\sigma$), note that a transition occurs for regimes 3 and 4 with a very slow decay of the related distributions. The development of small-scale wind-generated wave roughness over dominant waves combined with the pronounced fore-aft dominant wave crest asymmetry may explain this peculiar feature.

5.3. Curvatures

[21] Figure 12 displays in semi-logarithmic scales the normalized p.d.f. of wave curvature as well as for comparison, the normal and two-sided exponential distributions ($p(\gamma) = \exp(-2|\gamma|)$). Two specific behaviors can be distinguished for the various wave regimes. For regimes 1 and 2, the p.d.f. exhibit a marked asymmetry, with a peak shifted at small negative curvatures and a more pronounced tail at high positive curvatures. For the first regime, this shape can be explained by the main features of capillary-gravity waves exhibiting round crests and sharp troughs while for regime 2, it should be rather ascribed to the round bulge developing ahead the crest of gravity-capillary waves and the presence of parasitic capillaries with very sharp troughs. For longer wave fields observed in regimes 3 and 4, the curvature distributions are characterized by a striking triangular shape fitting closely the exponential curve at small to moderate curvatures (less than two standard deviations) and a slower but almost symmetric decrease at large curvatures. When examined the wave profiles, it comes out that small positive and negative curvature values can be associated to the flatness of the backward face of gravity-capillary or gravity waves and the large ones to the steepness of the wave fronts, then occasionally ruffled by large disturbances generated by microbreaking and breaking events. The fact that the curvature distributions at these regimes are far from the Gaussian behavior may suggest that this very asymmetric wave profile is a quite robust feature even when the wave steepness varies significantly within wave groups.

5.4. Cumulants

[22] The deviation from a Gaussian behavior of a random variable X is usually quantified in terms of cumulants. We recall that the cumulants κ_n are the coefficients in the series expansion of the logarithm of the characteristic function defined as follows (for any real variable u):

$$\log\langle\exp(\mathrm{iuX})\rangle = \sum_{\mathrm{n}=0}^{\infty} \frac{\kappa_{\mathrm{n}}}{\mathrm{n!}} (\mathrm{iu})^{\mathrm{n}}, \tag{2}$$

The cumulants can be expressed as a combination of moments of equal and lower orders. In general, the analysis is restricted to the first four cumulants which satisfy the following relationships:

$$\kappa_1 = \langle X \rangle, \tag{3}$$

$$\kappa_2 = \langle (X - \langle X \rangle)^2 \rangle, \tag{4}$$

$$\kappa_3 = \langle (X - \langle X \rangle)^3 \rangle, \tag{5}$$

$$\kappa_4 = \langle (X - \langle X \rangle)^4 \rangle - 3(\langle (X - \langle X \rangle)^2 \rangle)^2. \tag{6}$$

The first cumulant is the mean of the variable, the second is its variance. For a Gaussian variable, the higher cumulants vanish (i.e., $\kappa_n = 0$ when $n \geq 3$). The third-order cumulant κ_3 is related to the so-called skewness λ_3 of the random variable as follows:

$$\lambda_3 = \frac{\kappa_3}{\kappa_2^{3/2}}. \tag{7}$$

This dimensionless coefficient ranging between -1 and $+1$ is the main indicator of the asymmetry between positive and negative values. The fourth-order cumulant κ_4 is related to the so-called excess kurtosis λ_4 in a similar way, i.e.:

$$\lambda_4 = \frac{\kappa_4}{\kappa_2^2}. \tag{8}$$

When compared to a Gaussian distribution for which $\lambda_4 = 0$, let us just recall that a positive excess of kurtosis can be caused by a peaky distribution around zero and/or a frequent occurrence of large events.

[23] Table 1 summarizes the observed values of the first four cumulants for the different regimes. At first, one should note that the higher moments of a random variable are very sensitive to the largest values of its distribution. In that respect, we found rare but drastic occurrences of very large slopes and curvatures at the highest regimes, as shown for instance in Figures 4 and 5. These values are generally associated to either quasi-vertical wave fronts observed just prior to wave breaking or the presence of very steep surface disturbances generated at the bulge toe of microbreaking waves or following the breakdown of longer gravity wave crests. In both cases, to retrieve the slope and curvature details of surface profiles at such very small scales reveals to be challenging owing to the wave profile quantification inherent to this optical technique and the related smoothing procedure. One way to bypass this fundamental difficulty is to estimate the moments of the slope and curvature distributions only after applying a well-defined cut-off. Thus, for longitudinal slope distributions, we compute the moments of various order for two different slope thresholds (0.84 and 1.73, i.e., surface inclinations of 40 and 60 deg). For wave curvatures, we restricted the moment estimates to values lower than 1000 m^{-1}, the values higher being discarded because looking very unrealistic at this stage of the visualization technique development. Note that the slope and curvature rms values are only weakly affected by such cut-off procedure (in the most unfavorable case (regime 4), we found a difference of less than 4% between the rms values of curvature according to whether the cut-off is applied or not).

[24] In Table 1, the error margin has been evaluated by computing the wave profiles with a smoothing window standard deviation varying from 6.5 to 7.5 (i.e., with a difference of half a pixel on both sides of the value finally adopted). Accordingly, only the stable significant digits have been kept in the table.

[25] First, as expected, one can notice that the rms value of wave height increases rapidly with fetch and wind. For the quasi-Gaussian capillary-gravity wave regime (regime 1), the higher cumulants are also negligible. For the other regimes, the wave height skewness and kurtosis remain of same order of magnitude with $\lambda_3 \simeq +0.4$ and $\lambda_4 \simeq -0.3$. The positive skewness is mainly due to the vertical asymmetry between the sharp crests and the flat troughs which is classically observed for gravity waves of moderate to high steepness. This study shows that wind waves of decimeter scale can present such a nonlinear wave shape. However, for gravity-capillary wave fields or short gravity waves as observed in regimes 2 and 3, the parasitic capillaries or microbreaking disturbances which develop primarily on the forward face of the crests, may increase the vertical wave asymmetry and so, should contribute to the skewness magnitude too. The slightly negative excess of kurtosis indicates a weak dispersion of the values of elevation, by the fact that at small fetches the distribution is essentially controlled by the shape of dominant waves. Regarding the slope distribution, the rms value increases slowly with fetch and wind and is practically not sensitive to the chosen threshold for the maximum value. As mentioned previously, the skewness and kurtosis values, however, are very sensitive to this cut-off. The magnitude of skewness thus increases drastically with the threshold and can reach values close to -1. The skewness coefficient is stronger for regimes 2 and 3, where the asymmetry is more marked (see Figure 11). The negative sign of the skewness accounts for the horizontal asymmetry of the wave profiles, which are bent in the wind direction. The excess kurtosis increases with the threshold but remains moderate. As last, when examined the statistical properties of curvature, it is noteworthy to observe that the rms value is quasi-independent of wind and fetch, rating about 60–70 m^{-1} which corresponds to a radius of curvature of 1–2 cm. The skewness decreases with wind and fetch, which is the result of a stronger asymmetry in the small regimes. The kurtosis is very large, due to the slow decay of the distribution, which is seen to be closer to an exponential function rather than a Gaussian one.

6. Structure Functions of Wind Wave Fields

[26] These observations provides for the first time high resolution spatial measurements of wind wave height along a longitudinal section of 23 cm. Then, to investigate the two-point statistical properties of the different wind wave fields selected above present a special interest here, in particular in a perspective of improving surface modeling for radar remote sensing.

6.1. Autocorrelation and Related Functions

[27] For a (centered) random surface of elevation η, the two-point statistics are primarily described by the autocorrelation function C between two points x' and x'' defined as:

$$C(x', x'') = \frac{\langle \eta(x')\eta(x'') \rangle}{\left(\langle \eta^2(x') \rangle \langle \eta^2(x'') \rangle \right)^{1/2}}, \tag{9}$$

or alternatively, the (second-order) structure function given by the expression:

$$S_2(x', x'') = \langle (\eta(x') - \eta(x''))^2 \rangle. \tag{10}$$

The statistical features of a random surface are generally assumed to be invariant over translation, an hypothesis which is justified for short samples. In that case the two-point autocorrelation function depends only on the space lag $x = x' - x''$ and can be expressed by a single-variable function $C(x)$.

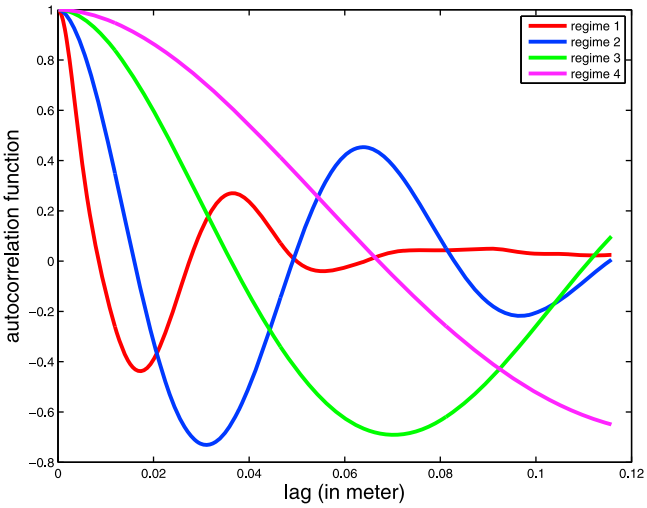

Figure 13. Wave height autocorrelation functions estimated for the four different wave regimes.

The classical technique for computing the autocorrelation function consists in estimating the spatial average of the product $\eta(x')\eta(x'+x)$ as follows:

$$\sigma^2 C(x) = \lim_{L\to\infty} \frac{1}{L} \int_{-L/2}^{L/2} \eta(x')\eta(x'+x)dx' \,, \qquad (11)$$

in which σ^2 is the variance of wave elevation. For short samples, i.e., for a wind wave field with a dominant wavelength of order of the profile length L (that means here $\lambda \approx$ 20 cm), the result is strongly biased. For the present data basis, however, we can take advantage of the profile time records to perform a further average over different realizations in time. In that way, the correlation function can be estimated from an average over the N available profiles recorded at the respective times t, using the expression:

$$\sigma^2 C(x'-x'') = \frac{1}{N}\sum_t \eta(x',t)\eta(x'',t), \qquad (12)$$

in which the number N of surface profiles ranges from 1800 to 3000, depending on the wind and fetch conditions. The "stationary" autocorrelation function $C(x)$ is thus obtained by further averaging the covariance function $C(x'-x'')$ over all doublets distant of the prescribed space lag $x = |x'-x''|$. Note that the estimation of $C(x)$ deteriorates at large space intervals because a fewer of adequate doublets is then found.

[28] The autocorrelation function is shown in Figure 13 for the different wind wave field regimes. As usually observed for the temporal autocorrelation function, this slowly decreasing space function oscillates with a "pseudo-period" approximately equal to the dominant wavelength. For spatially homogeneous wave fields, note that there is a trivial relationship between the structure and correlation functions, $S_2(x) = 2(C(0) - C(x))$, so that only the latter has been plotted.

[29] It is easier to investigate the self-similar nature of the wave profiles observed at the four typical regimes by rescaling the different autocorrelation functions by the respective dominant wavelength. To evaluate such scale, an estimation of the half of wavelength using the position of the first minimum has been chosen preferentially to a direct measurement of the "pseudo-period" (related to the position of the first maximum), the former being less affected by spurious effects introduced by the fast decrease of the autocorrelation function. As clearly seen in Figure 14, the autocorrelation functions for dominant gravity-like wind wave fields (regimes 2 to 4) collapse remarkably well into a single curve over almost one wavelength, at least within the uncertainties caused by the limited wave profile length. The autocorrelation function for the capillary-gravity wave field (regime 1) exhibits a very distinct behavior inasmuch as a much faster decrease is observed, noticeable even very close to zero. This can be interpreted readily as the manifestation in the physical space of the related broad peak spectral behavior found in the wave number space for such wave fields [*Caulliez and Collard*, 1999]. If we consider that the various autocorrelation functions decrease exponentially versus lag, then we can define a correlation length ζ as the distance for which the related exponential envelop reaches $\exp^{-1}$, i.e., a value of 0.37. Hence the dominant wavelength can be seen as a good indicator of the alongwise correlation length for wind wave fields observed at short fetches in laboratory.

[30] As inferred just above, the Fourier transform of the autocorrelation function is the so-called power spectrum, which is the most important and customary quantity in the characterization of random wind wave fields. It is usually estimated with the so-called periodogram technique, which consists in averaging the discrete Fourier transform of the profiles. However, this technique is not appropriate for short samples (i.e., smaller or just a little longer than the dominant wavelength), because it is compromised by the tilting effect of the sample-sized facet and the artificial singularities generated on both sides of the profile. To compute the Fourier transform of the stationary autocorrelation functions as estimated previously by an ensemble average may provide another possibility for such estimates. In fact, this method again is not optimal because the autocorrelation function

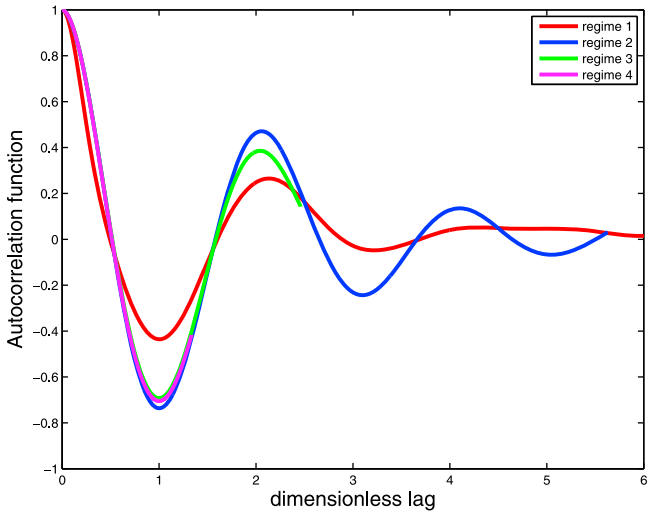

Figure 14. Rescaled wave height autocorrelation functions estimated for the four different wave regimes. The horizontal axis is scaled in units of the respective first minimum location, i.e., in units of the half of the dominant wave field wavelength.

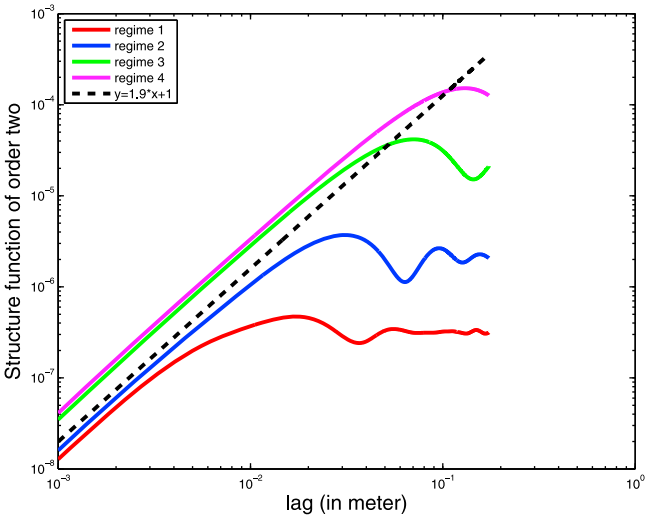

Figure 15. Wave height structure functions estimated for the four different wave regimes and plotted in logarithmic scales.

does not vanish at the maximal lag available (typically the profile length here) and so, must be tapered to avoid discontinuity effects at the edges. Furthermore, the autocorrelation function becomes less and less accurate at large lags, which induces an extra bias in the spectrum estimation.

[31] In order to determine precisely the spectral power-law decrease generally observed at small scales for wind wave fields (see, for instance, *Jähne and Riemer* [1990] for wind wave slope spectra), a better option may consist in studying directly the structure function at small lags. There is indeed a simple mathematical relationship [*Guérin et al.*, 1997] between the so-called local fractal exponent α of the structure function power increase (i.e., $S_2(x) \sim |x|^{\alpha}, x \to 0$) and the fall-off of the wave energy spectrum ($E(k) \sim |k|^{-\alpha-1}$). Figure 15 displays the structure functions as estimated for the four regimes and plotted in logarithmic scales. Thus, it is striking to see that these functions exhibit a similar power-law behavior over more than one or two decades starting in the millimeter range of scales (shorter scales are not relevant because they are affected by smoothing). The best fit to these straight curves allows to approximate quite accurately the structure functions by the expression $S_2(x) \sim |x|^{1.9}$, which corresponds to a $k^{-2.9}$ fall-off of the wave number spectra in this small-scale wave domain. The exponent of this power-law is very close to the -3 value as previously suggested in this wave number range by using dimensional analysis [*Phillips*, 1977].

6.2. Skewness and Kurtosis Functions

[32] Non-Gaussian characteristics of the increments of a random process are described by the two-points cumulants. Due to the limited field of view and limited accuracy available by the present visualization technique, we will restrict again our analysis to the third and fourth order cumulants, referred to as the skewness and kurtosis functions and respectively expressed by:

$$S_3(x', x'') = \langle (\eta(x') - \eta(x''))^3 \rangle \tag{13}$$

and

$$S_4(x', x'') = \langle (\eta(x') - \eta(x''))^4 \rangle. \tag{14}$$

The skewness and kurtosis functions turn out to have important implications in the calculation of the incoherent radar cross-section over a non-Gaussian rough surface. The former is responsible for the upwind-downwind asymmetry of the back-scattering diagram while the latter accounts for its shape.

[33] These functions however are increasingly difficult to determine quantitatively as they require more and more accuracy on the measured height differences. As previously, we assume that they are invariant under translation, so that they actually depend on space lag x with $x = x' - x''$. Note that $S_3(x)/x^3$ is the skewness of the slope distribution of the chords which connect every couple of points separated by a longitudinal distance x over the surface. The slope of such chords is mainly determined by surface oscillations of wavelength greater than x, so that the skewness function can be seen as the skewness of the filtered surface slopes. A similar interpretation holds for the kurtosis function.

[34] The skewness function for wind wave fields is poorly known presently and so, only speculations about his shape have been given in the literature. A few authors, such as *Chen et al.* [1992, 1993], suggest a cubic behavior at the origin. By considering a physical vanishing at large lags, they derive an expression of the form $S_3(x) \sim \alpha x^3 \exp(-\beta x^2)$. Such a trend is consistent with a first-order Taylor expansion of type:

$$S_3(x) \sim \langle (\eta_x)^3 \rangle x^3, \tag{15}$$

in the neighborhood of the origin and converges to zero at the infinity.

[35] As displayed in Figure 16 for the different wind wave fields, the estimated skewness functions consist in slowly decreasing oscillating functions with a first minimum approximately located at one fourth of the dominant wavelength. In this plot, note that a common renormalization factor $\kappa_2^{-3/2}(\eta)$ has been applied to get functions of similar order of magnitude across the regimes. To describe these functions, following

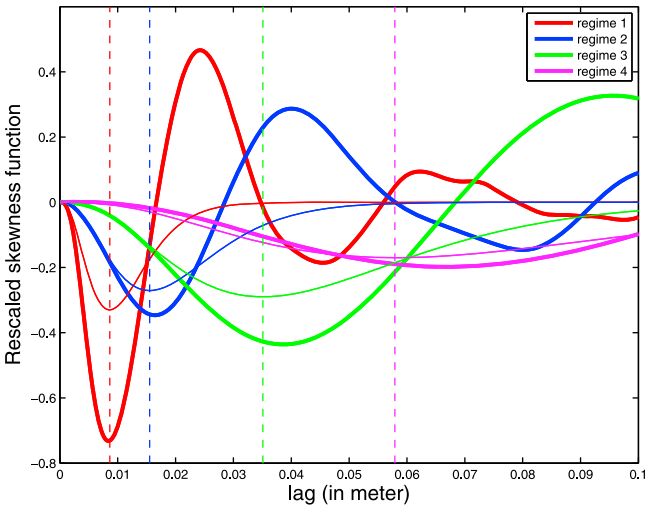

Figure 16. Rescaled wave height skewness functions estimated for the four different wave regimes and plotted together with the respective parametric curves given by equation (16) (thin lines). The vertical dashed lines indicate the respective position of one fourth of the dominant wavelength.

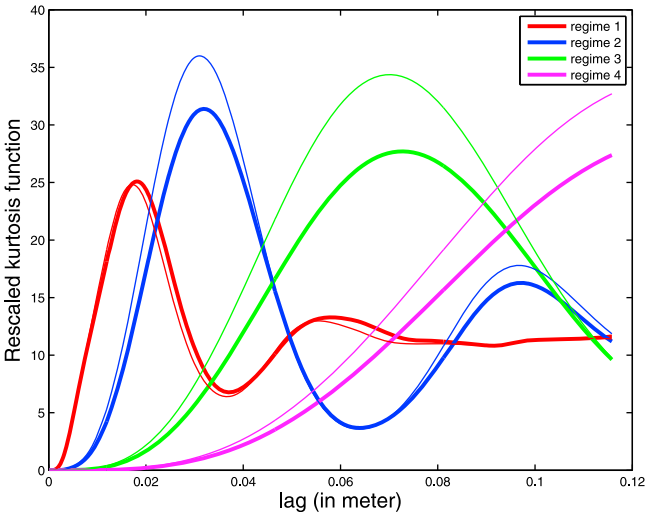

Figure 17. Rescaled wave height kurtosis functions estimated for the four different wave regimes and plotted together with the respective parametric curves given by equation (19) (thin lines).

Chen et al. [1992], several expressions based on an exponential, Gaussian or Weibull behavior at large lags, have been tested. Although any of these model functions might account for the observed oscillations, the best fit, in particular at short lags, is then given by the expression:

$$S_3(x) \sim ((\eta_x)^3)x^3 \exp(-12|x|/\lambda), \tag{16}$$

in which the exponential factor is chosen to prescribe the first extremum at one fourth of the dominant wavelength ($x = \lambda/4$), i.e., roughly at the first zero-crossing of the autocorrelation function. In fact, the Taylor expansion of the ratio S_3/x^3 around zero shows the occurrence of a dominant linear term in x, which favors the choice of an exponential rather than a Gaussian decrease in equation (16). No improvement however has been obtained when introduced a sine function in such a model equation. Even if not entirely satisfactory, the proposed expression with an exponential decrease at large lags thus proves to be by far the best, at least at short lags, contrarily to the model form postulated by *Chen et al.* [1992].

[36] The evolution with lag of the kurtosis function for the different wave regimes when estimated by the aforementioned expression and renormalized by a factor $\kappa_2^2(\eta)$, is reported in Figure 17. These functions look as oscillating damped functions around a constant value close to 12, but vanish at zero lag. Theoretically, the behavior of such functions is also *a priori* unknown but primarily, two specific constraints should be satisfied at each side of the variation domain. The behavior at the origin is imposed by the variance and kurtosis of slopes,

$$S_4(x)_{x\to 0} \sim \langle(\eta_x)^4\rangle x^4 \simeq (3 + \lambda_4(\eta_x))\kappa_2^2(\eta_x)x^4, \tag{17}$$

where the bias in slope $(\eta_x)^4$ has been neglected. The asymptotic value at large lags is related to the variance and kurtosis of wave heights, the latter being found close to 3,

$$S_4(x) \to 2\langle\eta^4\rangle + 6\left(\langle\eta^2\rangle\right)^2 \simeq 12\kappa_2^2(\eta). \tag{18}$$

Numerical tests clearly show that the extrema of the kurtosis functions are located at the same position as these of the respective structure functions. This fact combined with dimensional arguments strongly suggest that the kurtosis function might be essentially proportional to the square of the related structure function. Further numerical experiments then allow to check that the ratio S_4/S_2^2 is effectively maximum at zero, where it reach the kurtosis of longitudinal slope $(3 + \lambda_4(\eta_x))$, and minimum at the first zero-crossing of the autocorrelation function. In view of these well-identified features, the following expression can be proposed for modeling such function:

$$S_4(x) = 3 + \lambda_4(\eta_x)\exp(-12|x|/\lambda)S_2^2(x), \tag{19}$$

As expected, this model function exhibits a first maximum located at one half of the dominant wave and converge at large lags towards $12\kappa_2^2(\eta)$. The agreement between the theoretical curves and the kurtosis functions observed for each regime is then quite remarkable at short and large lags, as shown in Figure 17. Note that the excess kurtosis of longitudinal slope has been calculated using a threshold of 60 degrees to prevent from explosive values as discussed in section 5.

7. Conclusion

[37] An analysis of the one- and two-point statistical properties of wind wave fields as observed in laboratory has been carried out using high-resolution water surface profiles extracted from video camera images. In this study, we focus our attention on four well-identified types of wind wave fields in the range of centimeter to decimeter dominant wave scale and for which the respective role of the underlying physical processes controlled by gravity and capillary restoring forces varies. As a first and fundamental result, this work enables us to distinguish two very different behaviors in the statistical distribution of geometrical wave characteristics investigated here, i.e., wave height, longitudinal slope and curvature. They are associated on one hand to capillary-gravity wave fields (i.e., $\lambda \leq 6$ cm) and in the other hand but in a more surprising way, to the wind wave fields from gravity-capillary to short gravity scales (i.e., here, 6 cm $\leq \lambda \leq$ 25 cm). The statistical properties of these two types of wave fields differ essentially in the following way: in the capillary-gravity wave regime observed at very short fetch and moderate wind, the wave height distribution follows closely a normal distribution but strongly departs from it in the other gravity-type wave regimes. For the latter, the distribution has positive skewness and negative excess kurtosis, in respect of the fast decrease of the negative part of the distribution comparatively to the related Gaussian evolution. The precise skewness and kurtosis values are practically invariant with dominant wavelength and reach about 0.4 and -0.3, respectively. Let us just mention too that similarly to wave height, the distribution of longitudinal wave slope better fits a Gaussian curve for capillary-gravity wave fields, in particular for positive slope values, but departs significantly from it at large negative slope values ($\eta_x < -2\sigma$), following there the same trend as wind wave fields of larger scales.

[38] Apart from these capillarity-gravity wave field peculiarities observed in the first regime, the changes in wave dissipation regime manifest by any other distinctive signature

of the statistical properties. An explanation may be found in the fact that successive transitions from regime 2 to regime 4 are essentially characterized by the possible occurrence of an additional wave dissipation process, namely the generation of parasitic capillaries, wave microbreaking or wave breaking respectively, then making such transitions fundamentally smooth. The statistical properties of wind wave fields observed in these scale domains thus are primarily governed by the gravity-type nonlinear shape and wave group behavior of dominant waves.

[39] The other findings can be summarized as follows:

[40] 1. The wave slope distribution of wind wave fields of centimeter to decimeter scale generated at short fetches is characterized by a strong negative skewness due to the pronounced asymmetry between forward and backward crest wavefronts. However, for short gravity wave fields of wavelength longer than 10 cm about, the slope distribution also exhibit a very steep decay for moderate positive slope values and a much slower decrease for higher slope values. Such feature can be associated to the occurrence of small-scale surface disturbances generated by microbreaking and breaking phenomena. Consistently, the kurtosis value becomes very sensitive to the chosen or experimentally-fixed threshold value in slope when occurred microbreaking and breaking events.

[41] 2. These observations reveal that for steady wind wave fields observed at very short fetches, the standard deviation of longitudinal wave curvature is not strongly dependent on wind conditions as well as dominant wave scale. The curvature skewness exhibits positive values but its magnitude decreases when dominant waves develop with fetch and wind by the fact that the curvature distribution becomes more symmetric owing to the decrease in the occurrence of parasitic capillaries. Contrarily, the kurtosis that takes very large values for all wave field conditions, increases regularly, the distribution becoming quasi exponential when microbreaking and breaking events occur.

[42] 3. The self-similar behavior of wind wave fields of short gravity scale is evidenced by using an appropriate rescaling of the wave height autocorrelation function. The related structure functions are found to behave as $\sim x^{1.9}$ at small wave scales. This result reveals indirectly that the wave number height spectra decrease according to a power law in $\sim k^{-2.9}$.

[43] 4. The investigation of the trends followed by the wave height skewness and kurtosis functions enables us to propose parametric expressions for fitting the curves at small and large lags.

[44] **Acknowledgments.** This work was supported by grants from the Agence Nationale pour la Recherche (project ANR-09-BLAN-0232-01 SIMODE), the Centre National d'Etudes Spatiales (CNES, project TOSCA/SMOS-Ocean) and the Institut National des Sciences de l'Univers (INSU/CNRS, project LEFE-IDAO). Many thanks go to Victor Shrira for useful comments on the manuscript and Alain Laurence for his help in the preparation and set-up of experiments.

References

Bourlier, C. (2004), Azimuthal harmonic coefficients of the microwave backscattering from a non-Gaussian ocean surface with the first-order SSA model, *IEEE Trans. Geosci. Remote Sens.*, *42*(11), 2600–2611.

Bréon, F., and N. Henriot (2006), Spaceborne observations of ocean glint reflectance and modeling of wave slope distributions, *J. Geophys. Res.*, *111*, C06005, doi:10.1029/2005JC003343.

Caulliez, G. (2011), Wind wave breaking from micro to macroscale, in *Gas Transfer at Water Surface 2010*, pp. 151–163, Kyoto Univ. Press, Kyoto, Japan.

Caulliez, G., and F. Collard (1999), Oscillating crescent-shaped water wave patterns, *Phys. Fluids*, *11*, 3195–3197.

Chapron, B., V. Kerbaol, D. Vandemark, and T. Elfouhaily (2000), Importance of peakedness in sea surface slope measurements and applications, *J. Geophys. Res.*, *105*(C7), 17,195–17,202.

Chen, K., A. Fung, and D. Weissman (1992), A backscattering model for ocean surfaces, *IEEE Trans. Geosci. Remote Sens.*, *30*(4), 811–817.

Chen, K., A. Fung, and F. Amar (1993), An empirical bispectrum model for sea surface scattering, *IEEE Trans. Geosci. Remote Sens.*, *31*(4), 830–835.

Coantic, M., and P. Bonmarin (1975), The air-sea interaction simulation facility at the Institut de Mécanique Statistique de la Turbulence, *Atmos. Technol.*, *7*, 72–79.

Cox, C., and W. Munk (1954), Statistics from the sea surface derived from the sun glitter, *J. Mar. Res.*, *13*, 198–227.

Diorio, J. D., X. Liu, and J. H. Duncan (2009), An experimental investigation of incipient spilling breakers, *J. Fluid Mech.*, *633*, 271–283.

Elfouhaily, T., and C.-A. Guérin (2004), A critical survey of approximate scattering wave theories from random rough surfaces, *Waves Random Complex Media*, *14*(4), 1–40.

Engen, G., I. Friestad-Pedersen, H. Johnsen, and T. Elfouhaily (2006), Curvature effects in ocean surface scattering, *IEEE Trans. Antennas Propag.*, *54*(5), 1370–1379.

Ermakov, S., K. Ruvinsky, S. Salashin, and G. I. Freydman (1986), Experimental study of the generation of capillary-gravitational ripple by strongly nonlinear waves on the surface of a deep liquid, *Izv. Acad. Sci. USSR Atmos. Oceanic Phys., Engl. Transl.*, *22*(10), 835–842.

Ermakov, S., I. Sergievskaya, and Y. Shchegolkov (1997), Curvature of finite-amplitude gravity-capillary waves: Studies under laboratory conditions, *Izv. Acad. Sci. USSR Atmos. Oceanic Phys., Engl. Transl.*, *33*(3), 394–401.

Fedorov, A., W. Melville, and A. Rozenberg (1998), An experimental and numerical study of parasitic capillary waves, *Phys. Fluids*, *10*, 1315–1323.

Guérin, C.-A. (2002), Scattering on rough surfaces with alpha-stable non-Gaussian height distributions, *Waves Random Complex Media*, *12*(3), 293–306.

Guérin, C.-A., M. Holschneider, and M. Saillard (1997), Electromagnetic scattering from multi-scale rough surfaces, *Waves Random Media*, *7*(3), 331–349.

Huang, N., S. Long, C. Tung, Y. Yuan, and L. Bliven (1983), A non-Gaussian statistical model for surface elevation of nonlinear random wave fields, *J. Geophys. Res.*, *88*(C12), 7597–7606.

Huang, N., S. Long, L. Bliven, and C. Tung (1984), The non-Gaussian joint probability density function of slope and elevation for a nonlinear gravity wave field, *J. Geophys. Res.*, *89*(C2), 1961–1972.

Hung, L., and W. Tsai (2009), The formation of parasitic capillary ripples on gravity-capillary waves and the underlying vortical structures, *J. Phys. Oceanogr.*, *39*(2), 263–289.

Jähne, B., and K. Riemer (1990), Two-dimensional wave number spectra of small-scale water surface waves, *J. Geophys. Res.*, *95*(C7), 11,531–11,546.

Jessup, A. T., W. C. Keller, and W. K. Melville (1990), Measurements of sea spikes in microwave backscatter at moderate incidence, *J. Geophys. Res.*, *95*(C6), 9679–9688.

Joelson, M., and M. Néel (2008), On alpha stable distribution of wind driven water surface wave slope, *Chaos*, *18*, 033117, doi:10.1063/1.2955742.

Kudryavtsev, V., and J. Johannessen (2004), On effect of wave breaking on short wind waves, *Geophys. Res. Lett.*, *31*, L20310, doi:10.1029/2004GL020619.

Lange, P., B. Jähne, J. Tschiersch, and J. Ilmberger (1982), Comparison between an amplitude-measuring wire and a slope-measuring laser water wave gauge, *Rev. Sci. Instrum.*, *53*, 651–655.

Liu, Y., X. Yan, W. Liu, and P. Hwang (1997), The probability density function of ocean surface slopes and its effects on radar backscatter, *J. Phys. Oceanogr.*, *27*(5), 782–797.

Liu, Y., M. Su, X. Yan, and W. Liu (2000), The mean-square slope of ocean surface waves and its effects on radar backscatter, *J. Atmos. Oceanic Technol.*, *17*(8), 1092–1105.

Lukaschuk, S., S. Nazarenko, S. McLelland, and P. Denissenko (2009), Gravity wave turbulence in wave tanks: Space and time statistics, *Phys. Rev. Lett.*, *103*(4), 044501, doi:10.1103/PhysRevLett.103.044501.

Miles, J. (1962), On the generation of surface waves by shear flows. Part 4, *J. Fluid Mech.*, *13*(03), 433–448.

Mouche, A. A., B. Chapron, N. Reul, D. Hauser, and Y. Quilfen (2007), Importance of the sea surface curvature to interpret the normalized

radar cross section, *J. Geophys. Res.*, *112*, C10002, doi:10.1029/2006JC004010.
Nazarenko, S., S. Lukaschuk, S. McLelland, and P. Denissenko (2010), Statistics of surface gravity wave turbulence in the space and time domains, *J. Fluid Mech.*, *642*(1), 395–420.
Nosov, V., and S. Pashin (1990), The statistical characteristics of wind-created sea waves in gravity and capillary range, *Izv. Acad. Sci. USSR Atmos. Oceanic Phys., Engl. Transl.*, *26*(11), 1161–1169.
Nouguier, F., C.-A. Guérin, and B. Chapron (2010), Scattering from nonlinear gravity waves: The "choppy wave" model, *IEEE Trans. Geosci. Remote Sens.*, *48*(12), 4184–4192.
Nouguier, F., C.-A. Guérin, and G. Soriano (2011), Analytical techniques for the Doppler signature of sea surfaces in the microwave regime—II. Nonlinear surfaces, *IEEE Trans. Geosci. Remote Sens.*, *49*(12), 4920–4927.
Phillips, O. (1977), *The Dynamics of the Upper Ocean*, Cambridge Univ. Press, Cambridge, U. K.
Plant, W. (2003), A new interpretation of sea-surface slope probability density functions, *J. Geophys. Res.*, *108*(C9), 3295, doi:10.1029/2003JC001870.
Schooley, A. (1954), A simple optical method for measuring the statistical distribution of water surface slopes, *J. Opt. Soc. Am.*, *44*(1), 37–40.
Shaw, J., and J. Churnside (1997), Scanning laser glint measurements of sea-surface slope statistics, *Appl. Opt.*, *36*(18), 4202–4213.
Srokosz, M. (1986), On the joint distribution of surface elevation and slopes for a nonlinear random sea, with an application to radar altimetry, *J. Geophys. Res.*, *91*(C1), 995–1006.
Thompson, D., B. Gotwols, and W. Keller (1991), A comparison of Ku-band Doppler measurements at 20 incidence with predictions from a time-dependent scattering model, *J. Geophys. Res.*, *96*(C3), 4947–4955.
Tsai, W., and L. Hung (2010), Enhanced energy dissipation by parasitic capillaries on short gravity-capillary waves, *J. Phys. Oceanogr.*, *40*(11), 2435–2450.
Valenzuela, G. R. (1978), Theories for the interaction of electromagnetic and oceanic waves—A review, *Boundary Layer Meteorol.*, *13*, 61–85.
Van Gastel, K., P. Janssen, and G. Komen (1985), On phase velocity and growth rate of wind-induced gravity-capillary waves, *J. Fluid Mech.*, *161*, 199–216.
Vandemark, D., B. Chapron, J. Sun, G. Crescenti, and H. Graber (2004), Ocean wave slope observations using radar backscatter and laser altimeters, *J. Phys. Oceanogr.*, *34*, 2825–2842.
Voronovich, A., and V. Zavorotny (2001), Theoretical model for scattering of radar signals in Ku- and C-bands from a rough sea surface with breaking waves, *Waves Random Complex Media*, *11*(3), 247–269.
Walsh, E. J., D. C. Vandemark, C. A. Friehe, S. P. Burns, D. Khelif, R. N. Swift, and J. F. Scott (1998), Measuring sea surface mean square slope with a 36-GHz scanning radar altimeter, *J. Geophys. Res.*, *103*(C6), 12,587–12,601.
Wu, J. (1971), Slope and curvature distributions of wind-disturbed water surface, *J. Opt. Soc. Am.*, *61*, 852–858.
Wu, J. (1977), Directional slope and curvature distributions of wind waves, *J. Fluid Mech.*, *79*(03), 463–480.
Zhang, X. (1995), Capillary-gravity and capillary waves generated in a wind wave tank: Observations and theories, *J. Fluid Mech.*, *289*, 51–82.